Applied Thermal Engineering 280 (2025) 128087

Contents lists available at ScienceDirect

Applied Thermal Engineering

journal homepage: www.elsevier.com/locate/apthermeng

Research Paper

A 30-year radioisotope thermophotovoltaic system with a 100-watt output based on 500 W general purpose heat source

Hongyang Jia [a], Zhiheng Xu [a,b,*], Chao Chen [a], Xiaobin Tang [a,b,*]

[a] Department of Nuclear Science and Technology, Nanjing University of Aeronautics and Astronautics, Nanjing 211106, China
[b] Key Laboratory of Advanced Nuclear Technology and Radiation Protection, Ministry of Industry and Information Technology, Nanjing 211106, China

ARTICLE INFO

Keywords:
Radioisotope thermophotovoltaic
Multi-physics modeling
Long-term thermal performance
Efficiency degradation

ABSTRACT

This study presents a radioisotope thermophotovoltaic system based on 500 W general purpose heat source (GPHS) units, which addresses critical challenges in balancing the high efficiency and longevity of nuclear power. The system employs two GPHS units (with eight $^{238}PuO_2$ fuel pellets) as an energy source, coupled with spectral filters and InGaAs photovoltaic arrays for energy conversion. A multi-physics coupled model integrating finite element analysis for thermal radiation simulations and computational modeling for photovoltaic algorithms demonstrates an initial overall system efficiency of 21.3 %, with component efficiencies of 84.0 % (emitter), 70.9 % (spectral filter), and 35.7 % (photovoltaic cells). The results reveal an annual efficiency degradation rate of 0.21 %, primarily driven by an emitter temperature decline (−144.6 ℃ over 50 years) and radiative flux reduction (419.7 → 204.3 W). A hybrid degradation model quantifies the synergistic effects of radioisotope decay and material aging, predicting a 30-year reliability threshold (reliability = 0). This study proposes thermal-optical-electrical coupling optimization methods and a longevity assessment framework for 100-watt-scale nuclear power systems.

1. Introduction

The demand for highly reliable power supplies for deep-space exploration missions and extreme environmental conditions has significantly increased the research and development of radioisotope power systems based on radioactive decay energy [1–4]. Radioisotope thermoelectric generators (RTGs) have been widely recognized as reliable power sources for long-duration space missions owing to their capability to deliver consistent energy over extended periods [5,6]. RTGs convert heat generated by radioactive decay into electricity using thermoelectric materials [7–9]. However, their energy conversion efficiencies remain relatively low, typically between 6 and 8 % [10,11]. Subsequently, a radioisotope thermophotovoltaic (RTPV) system based on a radioisotope heat source for energy conversion was proposed [12]. This type of power generation device has a theoretical efficiency greater than 40 % and has attracted widespread attention in recent years. RTPV systems utilize heat from radioactive decay to produce light, which is subsequently converted into electricity by photovoltaic (PV) cell arrays [12].

Recent research on RTPV system has predominantly focused on component-level optimizations and innovations, including radioisotope heat source design optimization, material selection and structural refinement of emitter or filter components, spectral matching optimizations, and investigations of thermal stability and radiation-induced damage mechanisms. Cheon et al. [13] demonstrated that an RTPV system utilizing cylindrical heterogeneous $^{238}PuO_2$ sources achieved 5–11 % lower radiation doses and more uniform thermal distributions compared to cubic homogeneous designs, as validated by ORIGEN-S, MCNP6/MAVRIC shielding analyses, and COMSOL thermal simulations. Cotfas et al. [14] experimentally demonstrated that increasing the temperature (25–87 °C) significantly impacted commercial PV cells, with the maximum power (P_{max}) decreasing by 0.14–0.47 %/℃ and the open-circuit voltage (V_{oc}) exhibiting negative temperature coefficients, necessitating irradiation-dependent correction models to optimize performance under high-temperature conditions. Sun et al. [15] demonstrated that elevated temperatures significantly degraded PV performance, with V_{oc} and maximum power (P_{max}) decreasing by 0.14–0.47 %/℃ due to the bandgap reduction and enhanced carrier recombination. Although the short-circuit current (J_{sc}) exhibited a minor increase, it failed to counteract the overall efficiency loss. Notably, multijunction cells (InGaP/InGaAs/Ge, temperature coefficient: −0.14 %/℃) and amorphous silicon (−0.18 %/℃) exhibit superior thermal stability compared to crystalline silicon (−0.47 %/℃), highlighting the material-dependent sensitivity in high-temperature

* Corresponding authors at: Department of Nuclear Science and Technology, Nanjing University of Aeronautics and Astronautics, Nanjing 211106, China.
E-mail addresses: xuzhiheng@nuaa.edu.cn (Z. Xu), tangxiaobin@nuaa.edu.cn (X. Tang).

https://doi.org/10.1016/j.applthermaleng.2025.128087
Received 3 April 2025; Received in revised form 13 August 2025; Accepted 26 August 2025
Available online 6 September 2025
1359-4311/© 2025 Elsevier Ltd. All rights are reserved, including those for text and data mining, AI training, and similar technologies.

Nomenclature

Q_R	Thermal power of the radioisotope, W
Q_e	Radiative heat flux emitted of the emitter, W
Q_f	Radiative heat flux through the filter, W
P_c	Electrical output power generated by the cell arrays, W
$\eta_{emitter}$	Emitter efficiency, %
η_{filter}	Filter efficiency, %
η_{cell}	Cell efficiency, %
η_{RTPV}	System efficiency, %
Q_0	Initial power of the heat source
$T_{1/2}$	Half-life of Pu-238
ρ	Density, kg/m^3
C_p	Specific heat capacity, J/(kg·K)
q	Heat flux by conduction, W/m^2
Q	Heat sources, W/m^3
T_e	Temperature of the emitter, ℃
T_c	Temperature of the cell arrays, ℃
h	Planck's constant, J·s
k	Boltzmann's constant, J/K
A_e	Surface area of the emitter, m^2
A_c	Surface area of the cell, m^2
$\varepsilon_e(\lambda)$	Emissivity of the emitter, –
$R_f(\lambda)$	Reflectance of the filter, –
$\phi_p(\lambda)$	Photon flux of the cell, W
$\phi_e(\lambda)$	Electron flux of the cell, W
$Q(\lambda)$	Quantum efficiency of the cell, –
J_{sc}	Short-circuit current of the cell, A
V_{oc}	Open-circuit voltage of the cell, V
J_0	Saturation current density of the cell, A
FF	Fill factor of the photovoltaic cell, –
E_g	Bandgap of the photovoltaic cell, eV
P_{max}	Maximum output electric power of the cell, W
P_{limit}	Minimum operating power of the system, W
RTG	Radioisotope thermoelectric generator
RTPV	Radioisotope thermophotovoltaic
GPHS	General purpose heat source
GIS	Graphite impact shell
FWPF	Fine-weaved pierced fabric
CBCF	Carbon-bonded carbon fiber
PV	Photovoltaic

environments.

Current research on RTPV systems has a limited focus on holistic structural configurations, despite the critical influence of system-wide heat transfer dynamics, component-level energy conversion efficiencies, and temperature distributions across emitters and PV cell arrays on the electrical power output. Radioisotope decay-induced temperature variations in fuel pellets and emitters directly degrade the system efficiency and electrical output. Current research on RTPV systems has failed to systematically correlate the thermal transport processes with the electrical power generation outputs. This critical research gap necessitates the development of a multi-physics computational framework that couples the nuclear heat transfer, spectral radiation, and PV conversion mechanisms coherently. Such an integrated model enables the concurrent optimization of thermal management and energy harvesting pathways, which is particularly crucial for spaceborne systems requiring decade-level operational stability under constrained mass budgets.

This study presents a 30-year RTPV system with 100-watt-scale output built upon a 500 W GPHS, systematically investigating the energy conversion mechanisms and long-term thermal performance evolution through multi-physics coupled modeling and the research framework is presented in Fig. S1. The system integrates stacked $^{238}PuO_2$ GPHS modules with spectral filters and InGaAs PV cell arrays to enable three-dimensional energy transfer, achieving an initial efficiency of 21.3 %. In the PV degradation model, the system maintains stable operation for 20 years with a reliability greater than 0.48, theoretically achieving a maximum service life of 30 years.

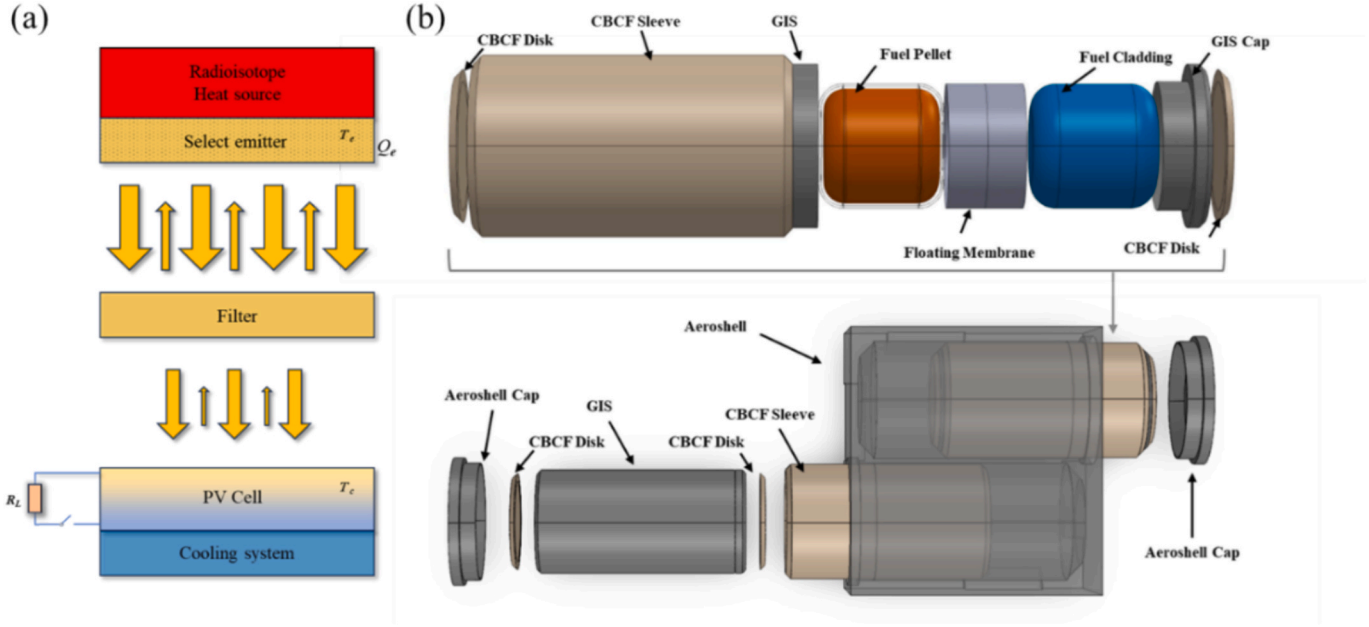

Fig. 1. (a) Schematic of the working principle of the RTPV system; (b) heat source structure diagram of the GPHS.

2. Principles and geometric configuration of the RTPV system

2.1. Energy conversion process and GPHS configuration

Fig. 1a shows the main components and operational mechanism of the RTPV system. The $^{238}PuO_2$ radioisotope heat source primarily undergoes alpha decay, releasing α-particles with an energy of 5 MeV [16]. The deposited energy from α-particle deceleration through inelastic collisions with fuel matrices generates thermal energy via ionization losses. This thermal energy elevates the emitter temperature, which then radiates infrared energy.

A spectrally selective filter is strategically positioned between the emitter and PV cell arrays to optimize the radiation spectrum [17]. This spectral management device selectively absorbs photons in wavelength regimes that are non-convertible by the PV semiconductor material while redirecting the corresponding energy flux back to the emitter through photon recycling [18,19]. Subsequently, spectrally optimized photons within the operational bandwidth of the PV cell are effectively harvested for carrier generation, thereby enabling enhanced thermophotovoltaic conversion through spectral reshaping and waste energy recuperation [20]. This energy conversion approach theoretically achieves a high efficiency and demonstrates robustness against external environmental factors, making it a promising solution for deep-space exploration applications [12].

The GPHS is the most successful and widely utilized radioisotope heat source and has been deployed in a diverse array of space exploration missions [21]. The concept of the GPHS dates back to 1976, when it was designed by the Los Alamos National Laboratory (LANL) [22]. To enhance the safety of radioisotope heat sources, studies have improved the overall performance of the fuel material $^{238}PuO_2$ and developed a robust and reliable fuel cladding. Furthermore, the thermal performance of the heat source was optimized by comprehensively considering the materials, dimensions, structures, and masses of its components. Extensive analyses and experimental validations were performed throughout the development of the GPHS, ultimately leading to the design shown in Fig. 1b.

Each GPHS module contains four $^{238}PuO_2$ fuel pellets capable of generating 250 W of thermal power during their initial operational life [12]. These fuel pellets are encapsulated within a high-strength, highly ductile DOP-26 iridium alloy cladding [23] to form a fuel cladding. The graphite impact shell (GIS) [24], fabricated from fine-weaved pierced fabric (FWPF) graphite, contains two fuel claddings separated by floating membranes and secured with a GIS cap, demonstrating exceptional energy absorption capabilities under accidental impact conditions.

The third layer, composed of carbon-bonded carbon fiber (CBCF) graphite, functions as a thermal insulation material, mitigating the effects of high external temperatures during re-entry. The CBCF sleeve is positioned coaxially outside the GIS with two CBCF graphite disks affixed to each end of the GIS using a graphite adhesive. The outermost layer, known as the aeroshell, is also made of high-strength and high-thermal-conductivity FWPF graphite, which ensures structural integrity while serving as an ablative layer. All the components are enclosed within the aeroshell and sealed with an aeroshell cap. Locking screws prevent loosening of the aeroshell cap during launch vibrations, and locking elements are employed to restrict the lateral relative motion during stacking. Except for the CBCF disks attached to the ends of the GIS, small gaps exist around the components [24,25]. In a vacuum environment, these gaps significantly reduce thermal conduction between the components, making surface-to-surface radiation the dominant mode of heat transfer [24].

The GPHS contains internal clearance gaps, with the geometric parameters of these gaps derived from previous studies. The surface-to-surface radiation heat transfer was identified as the primary heat transfer mechanism within these gaps. The computational framework employed COMSOL Multi-physics software to solve the solid heat transfer and surface-to-surface radiation equations simultaneously.

2.2. Geometry and materials of the RTPV system

The RTPV system configuration is illustrated in Fig. 2. Fig. 2a illustrates the primary assembly, including the main system components and cooling module, and Fig. 2b shows the structural layout of the core section. Two GPHS units with an initial thermal power of 500 W are positioned at the center. High-temperature-resistant, low-thermal-conductivity interfaces [26] are installed at both ends of the heat sources to minimize thermal losses, complemented by robust ceramic [27,28] support plates that provide structural integrity.

The emitter [29] is integrated around the GPHS perimeter with a two-dimensional periodic spectral filter positioned between the emitter and PV cell arrays. PV cells employ InGaAs semiconductor materials [30], which are selected for their superior infrared photon absorption and conversion efficiency.

Fig. 3 shows the quantitative evaluations, including the PV cell quantum efficiency, emitter emissivity, spectral reflectivity/transmissivity characteristics of the filter and alumina emissivity. More detailed datasets are provided in Supporting Information Figs. S1, S2, S3, and S4. The emitter exhibits high emissivity (peak ~ 0.95) in the 0.5–2.2 μm wavelength range, which represents its primary energy output spectrum. The InGaAs photovoltaic cell can absorb photons in the 0.4–2.2 μm range, demonstrating significant spectral overlap with the emitter's high-emissivity band. The filter further enhances system efficiency by maintaining high transmittance in this critical range (0.4–2.2 μm), allowing photons to pass through to the photovoltaic component. In other wavelength bands, the filter shows high reflectivity and low transmittance, which prevents low-energy photons from entering the cell and reflects them back to the emitter. This mechanism helps maintain the emitter's temperature while minimizing energy loss, thereby improving overall system efficiency.

3. Modules

3.1. Analysis of the RTPV system energy transport

The overall conversion efficiency of the RTPV system is governed by the interplay of the conversion efficiencies across various energy transformation stages.

$$\eta_{RTPV} = \frac{Q_e}{Q_R} \times \frac{Q_f}{Q_e} \times \frac{P_c}{Q_f} = \eta_{emitter} \times \eta_{filter} \times \eta_{cell} \tag{1}$$

where Q_R denotes the thermal power produced by the radioactive decay of the radioisotope, and Q_e represents the net radiative heat flux emitted by the emitter. Furthermore, Q_f signifies the radiative heat flux through a filter incident on the InGaAs PV cell arrays and P_c corresponds to the electrical output power generated by the InGaAs cell. Q_R is given as follows:

$$Q_R = Q_0 \cdot \exp\left(-\ln 2 / T_{1/2}\right) \tag{2}$$

where Q_0 is the initial power of the heat source and $T_{1/2}$ is the half-life of Pu- 238 [5].

The emitter efficiency $\eta_{emitter}$ is defined as the ratio of the radiant heat flux emitted from the surface of the emitter to the total energy generated by the radioactive decay of the isotope. This parameter quantifies the energy conversion efficiency between the radioisotope heat source and heat emitter and serves as a critical factor in enhancing the energy transfer efficiency of the entire system. The filter efficiency η_{filter} represents the respective energy conversion efficiency, accounting for energy losses during the heat transfer process. Similarly, the PV efficiency of the cell η_{cell} is defined as the ratio of the electrical energy output of the cell to the radiant heat flux incident on its surface. The overall efficiency of the RTPV system is the product of the individual efficiencies of these energy

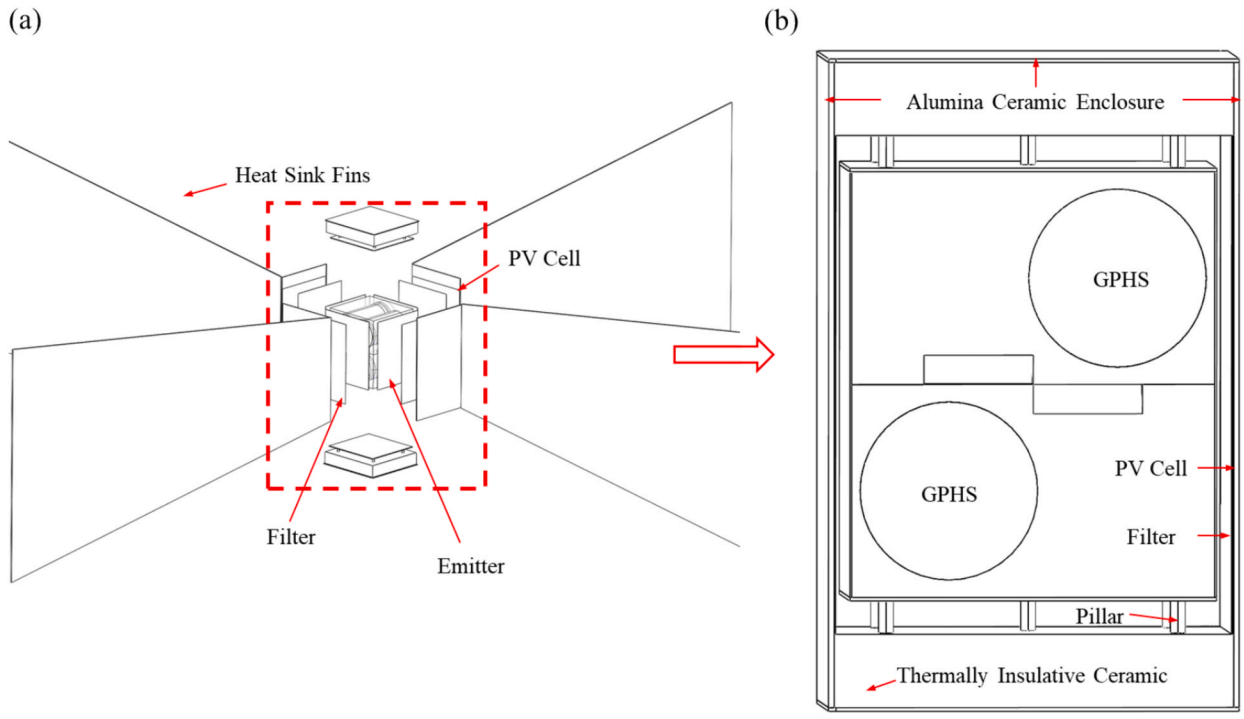

Fig. 2. Geometric configuration schematic of the RTPV system: (a) main system components; (b) structural layout of the core section.

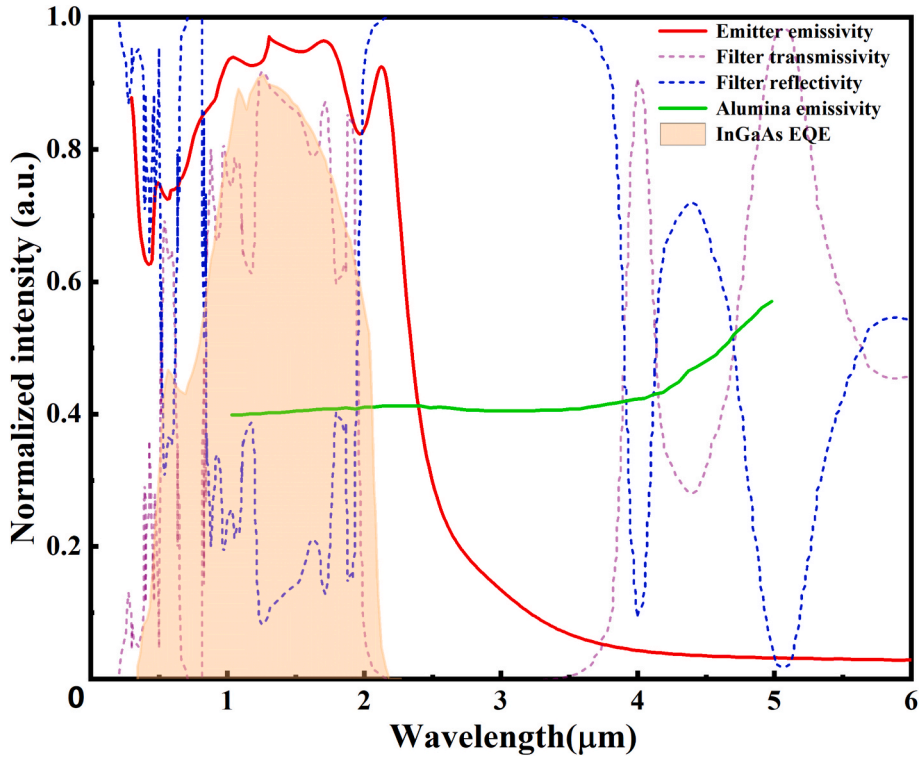

Fig. 3. Material parameters of the main components of the RTPV system.

conversion processes, emphasizing the interdependence of the performance of each component on the overall energy conversion effectiveness of the system.

3.2. Equations and parametric configuration

The RTPV system integrates two key heat transfer mechanisms: solids and surface-to-surface radiation. This dual-physics coupling enables a more accurate simulation of the energy transfer pathways within the system under real-world operating conditions. Surface-to-surface radiation heat transfer is specifically considered owing to the presence of gaps between the components in the GPHS module. These gaps significantly reduce the effectiveness of solid conduction, making radiative heat transfer the dominant mode of energy exchange between

adjacent components. The distinction between these heat transfer mechanisms critically influences the overall energy transfer efficiency of the RTPV system, underscoring the importance of accurately modeling the radiative heat transfer to optimize system performance. The multi-physics governing equations are detailed in the Supporting Information.

In the calculation of GPHS, the external boundary condition was set to the module surface radiating to the environment with an ambient temperature of 1060.4 ℃. At the time of the RTPV system, the radiator was replaced with an external surface temperature of 10℃. These equations were solved on a finite element mesh in COMSOL Multi-physics software and then used to obtain the temperature, heat radiation flux, and other numerical solutions. Mesh independence tests were performed for all the cases considered and showed that the mesh independence of the results of the mesh calculations used in the modeling was within 0.1 %.

3.3. Spectral energy propagation and battery power calculation

When the temperature of the heat emitter is T_e, the equation for the radiative spectral flux Q_e of the PV radiation radiated outward by the emitter [31] is as follows:

$$Q_e = \iint_{\lambda}^{\lambda+\Delta\lambda} \varepsilon_e(\lambda) \frac{2\pi hc^2\lambda^{-5}}{\exp(hc/\lambda kT_e) - 1} d\lambda dA_e \tag{3}$$

where $\varepsilon_e(\lambda)$ is the emissivity of the emitter, h is Planck's constant, k is Boltzmann's constant, and c is the speed of light. A_e denotes the emitter area. Q_f is the radiation flux through the optical filter, which is assumed to be the radiated spectral flux Q_c reaching the surface of the PV cell arrays, as follows:

$$Q_c = \iint_{\lambda}^{\lambda+\Delta\lambda} \frac{2\pi hc^2\lambda^{-5}[\exp(hc/\lambda kT_e) - 1]^{-1}}{[\varepsilon_e(\lambda)]^{-1} + \left\{[R_f(\lambda)]^{-1} - 1\right\}^{-1}} d\lambda dA_c \tag{4}$$

The energy flux absorbed by the PV cell arrays is in the form of photons. As each photon has an energy $h\nu = hc/\lambda$, the absorbed photon flux $\phi_p(\lambda)$ is given as follows:

$$\phi_p(\lambda) = \iint_{\lambda}^{\lambda+\Delta\lambda} \frac{2\pi c\lambda^{-4}[\exp(hc/\lambda kT_e) - 1]^{-1}}{[\varepsilon_e(\lambda)]^{-1} + \left\{[R_f(\lambda)]^{-1} - 1\right\}^{-1}} d\lambda dA_c \tag{5}$$

where A_c denotes the area of the PV cell arrays. The PV cell arrays convert the absorbed photons into an electron flux ϕ_e with a wavelength-dependent quantum efficiency $Q(\lambda)$, as follows:

$$\phi_e = \iint_{\lambda}^{\lambda+\Delta\lambda} \phi_p(\lambda) Q(\lambda) d\lambda dA_C \tag{6}$$

Therefore, short-circuit current J_{sc} of the cell is as follows:

$$J_{sc} = e\int_0^{\infty} \phi_e(\lambda) d\lambda \tag{7}$$

The open-circuit voltage V_{oc} of the PV cell is as follows:

$$V_{oc} = (kT_c/e)\ln[(J_{sc}/J_0) - 1] \tag{8}$$

The fill factor FF of the cell is as follows:

$$FF = \left\{1 - [\ln(J_{sc}/J_0)]^{-1}\right\}\left\{1 - \ln[J_{sc}/J_0][\ln(J_{sc}/J_0)]^{-1}\right\} \tag{9}$$

$$J_0 = \left[2.555 \times 10^{-4} T_c^3 \exp(-E_g/kT_c)\right] \tag{10}$$

where J_0 is the saturation current density, E_g is the bandgap width of the InGaAs, T_c is the cell temperature, and e denotes the electronic charge. The bandgap E_g and maximum output power P_{max} for the InGaAs cell arrays are as follows:

$$E_g = 0.564 - 3.7^{-4} \times (T_c - 300) \tag{11}$$

$$P_{max} = J_{sc} V_{oc} FF \tag{12}$$

By applying these equations, a sophisticated electrical power output model for PV modules can be established within the MATLAB environment, enabling a comprehensive simulation and analysis of their performance across diverse operational scenarios.

3.4. PV cell attenuation model

Photovoltaic components in the RTPV system primarily undergo three core degradation mechanisms: radiation-induced damage, where long-term exposure to α-particles from ^{238}Pu decay and secondary radiation creates lattice defects in the semiconductor, reducing carrier mobility and quantum efficiency, thereby lowering short-circuit current and open-circuit voltage; encapsulant aging, as materials like EVA undergo browning and adhesion loss under prolonged UV radiation and humidity, decreasing light transmittance to the active layer and reducing absorbed photon flux; and inhomogeneous degradation, where manufacturing quality variations lead to uneven aging across the array, broadening the power distribution and increasing standard deviation [32].

In this study, a hybrid degradation model was used to characterize the power decay of PV arrays, incorporating both radioactive effects and long-term material aging mechanisms. The mathematical framework comprises three core components, as follows:

$$m(t) = P_c - A \cdot t \tag{13}$$

where A denotes the degradation rate. The exponential term captures the intrinsic decay of the radionuclide-induced thermal contributions, whereas the linear term accounts for the cumulative environmental and operational stressors.

The decay of P_c over time adheres to an exponential decay pattern, with the analysis yielding a fitted curve expressed as follows:

$$P_c(t) = 107.36 \cdot \exp(-0.029 \cdot t) \tag{14}$$

To address the stochastic performance dispersion, the standard deviation $\sigma(t)$ of the power distribution increases linearly over time, as follows:

$$\sigma(t) = \sigma_0 + B \cdot t \tag{15}$$

where σ_0 is the initial standard deviation, and B quantifies the annual growth rate of variability, reflecting inhomogeneous aging across PV cells. σ_0 is calculated as follows:

$$\sigma_0 = P_c(t) \cdot B \tag{16}$$

At any time t, the instantaneous power $P(t)$ is assumed to follow a Gaussian distribution, as follows:

$$p(P,t) = \frac{1}{\sqrt{2\pi}\cdot\sigma(t)} \exp\left(-\frac{(P - m(t))^2}{2\sigma(t)^2}\right) \tag{17}$$

The reliability $R(t)$, which is defined as the probability that the power exceeds a critical threshold P_{limit}, is derived from the cumulative distribution function of $p(P, t)$, as follows:

$$R(t) = 1 - \Phi\left(\frac{P_{limit} - m(t)}{\sigma(t)}\right) \tag{18}$$

This formulation enables probabilistic predictions of power thresholds and reliability metrics to be calculated.

A comprehensive model incorporating both radioisotope heat source decay and PV module degradation can be established using Equations (13)-(18). In this model, parameters A, B [32], and P_{limit} were referenced from the literature as 0.005, 0.0167, and 53.15 W, respectively. The

selection of parameters *A*, *B*, and P_{limit} in the photovoltaic module degradation model is rooted in data-driven principles and scenario-specific adaptability. Parameter *A* characterizes the annual linear degradation rate of PV modules, derived from a comprehensive review of global field studies indicating a typical range of 0.3 % to 3 % per year, with 0.5 % emerging as the most representative value for contemporary technologies. Parameter *B* quantifies the annual growth rate of the standard deviation in power distribution, based on empirical observations such as the doubling of standard deviation over an 11-year period, which is consistent with manufacturing tolerances and physical constraints. P_{limit}, referencing industry practices, is tailored to specific system requirements to ensure accurate failure prediction. Collectively, these parameters encapsulate intrinsic degradation patterns and fulfill the demands of practical reliability assessment.

These mechanisms are systematically addressed by the hybrid degradation model: the exponential term accounts for radiation effects indirectly through radioisotope decay-induced thermal changes, the linear term incorporates encapsulant aging-driven linear power loss, and parameter *B* quantifies inhomogeneous degradation, ensuring the model robustly captures real-world degradation behaviors.

4. Results and discussion

4.1. Thermal analysis of the GPHS

Fig. 4 illustrates the temperature distribution results of the GPHS components and Table 1 lists the comparative data with prior computational studies. The maximum temperature discrepancy between the simulation results and reference values was within 14℃, corresponding to a relative variance of less than 1 %, demonstrating excellent consistency. The mesh configuration of the GPHS is presented in Fig. 5, where the geometric structure is discretized based on the refinement requirements of different regions.

As shown in Table 2, the computational results exhibited minimal sensitivity to mesh density variations. Specifically, the numerical solutions showed consistent agreement (within 0.1 % relative deviation) across multiple computational iterations with varying mesh resolutions (ranging from 3.9×10^5 to 1.0×10^6 elements). This mesh-independence validation confirmed the mathematical robustness of the proposed thermal source modeling methodology and the geometric rationality of the meshing strategy adopted for the GPHS simulation. The grid independence verification of the RTPV system is presented in Table S1 of the supplementary materials.

Table 1
Comparison of calculated and reported temperature values for the GPHS module.

Parameters	Temperature Presented (℃)	Temperature Reported (℃)	Difference	Relative Deviation (%)
Fuel Pellet Max	1442.8	1456.0	−13.2	−0.91
Fuel Pellet Average	1346.0	1347.0	−1.0	−0.07
Fuel Cladding	1258.6	1271.0	−12.4	−1.00
GIS Inner Surface	1173.2	1183 0.0	−9.8	−0.84
GIS Outer Surface	1170.0	1180.0	−10.0	−0.85
CBCF Sleeve Inner Surface	1151.5	1161.0	−9.5	−0.83
CBCF Sleeve Outer Surface	1095.8	1096.0	−0.2	−0.02
Aeroshell Inner Surface	1075.8	1076.0	−0.2	−0.02
Aeroshell Outer Surface	1076.0	1074.0	2.0	0.19

The RTPV system was simulated using COMSOL Multi-physics software with coupled solid heat transfer and surface-to-surface radiation modules, and the hemicube method was implemented for radiative exchange calculations. The key structural parameters listed in Table 3 were extracted from published literature [33]. The thermal analysis results from COMSOL Multi-physics software were subsequently interfaced with MATLAB software for PV output power calculations using custom-developed algorithms.

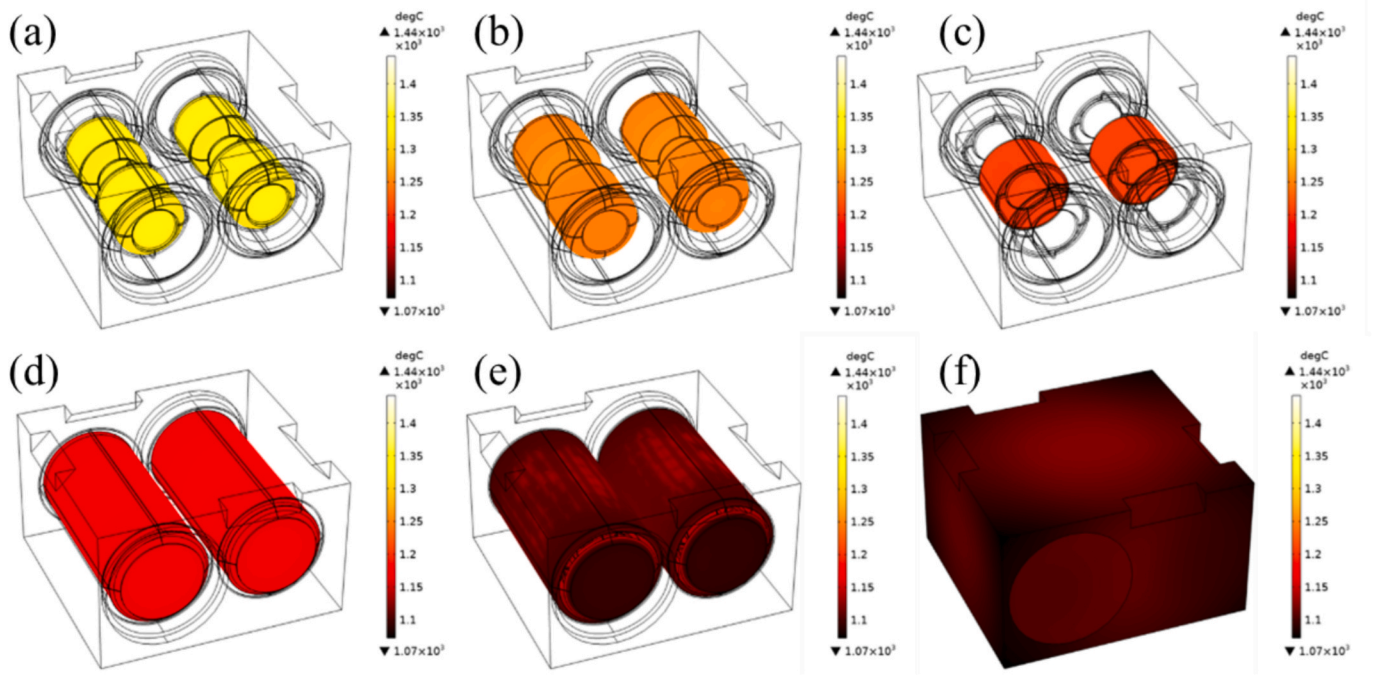

Fig. 4. Temperature distributions of GPHS module components: (a) fuel pellet, (b) fuel cladding, (c) floating membranes, (d) GIS, (e) CBCF, (f) aeroshell.

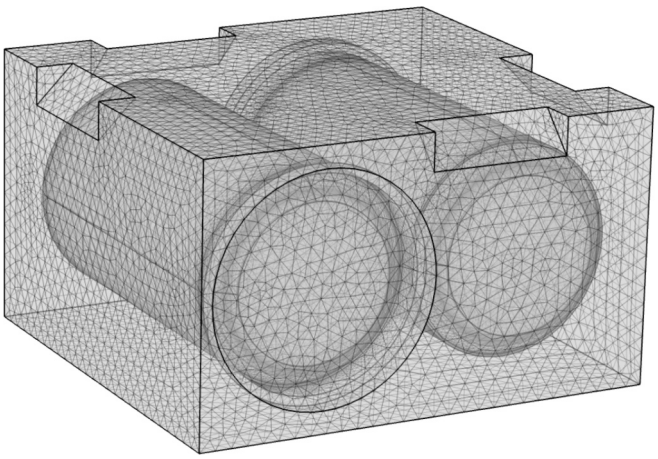

Fig. 5. Numerical mesh grid implemented in the thermal analyses of the GPHS modules.

Table 2
Computational results under different mesh densities.

Set	1	2	3	4	5
Mesh Number	3.9 × 10^5	4.4 × 10^5	5.2 × 10^5	8.3 × 10^5	1.0 × 10^6
Fuel Pellet Max, ℃	1440.5	1440.8	1440.6	1440.6	1440.8
Fuel Pellet Average, ℃	1345.9	1346.0	1346.0	1346.0	1346.1
Fuel Cladding, ℃	1258.6	1258.6	1258.6	1258.7	1258.6
GIS Inner Surface, ℃	1173.2	1173.2	1173.0	1173.1	1173.1
GIS Outer Surface, ℃	1170.1	1170.0	1170.0	1170.0	1170.1
CBCF Sleeve Inner Surface, ℃	1151.3	1151.5	1151.3	1151.3	1151.4
CBCF Sleeve Outer Surface, ℃	1095.6	1095.5	1095.6	1095.6	1095.5
Aeroshell Inner Surface, ℃	1075.7	1075.8	1075.8	1075.8	1075.8
Aeroshell Outer Surface, ℃	1076.2	1076.0	1076.2	1076.2	1076.2

Table 3
Structural parameters of RTPV system components.

Component	Geometric Parameters (mm)
GPHS	99.57 × 93.17 × 58.17
Emitter	116.34 × 94.17
	116.34 × 99.57
Filter	136.34 × 108.57
	136.34 × 102.17
PV cell array	136.34 × 108.57
	136.34 × 102.17
Support Pillars	Φ4 × 9
Thermally Insulative Ceramic	109.57 × 103.17 × 20

The initial operational characteristics of the RTPV system are presented in Table 4. The key energy fluxes include an emitter radiative flux (Q_e) of 419.7 W and a radiative heat flux through a filter (Q_f) of 297.7 W, yielding a 106.3 W electrical output (P_c) from the InGaAs photovoltaic array. The fuel pellets with a total power output of 500 W experience an energy loss of approximately 80.3 W during thermal transfer to the emitter. The model inspection revealed that this energy loss primarily occurred through thermal dissipation in the upper and lower thermal insulation ceramics of the GPHS.

Table 4
RTPV system thermal analysis results.

Parameters	Results
T_e, ℃	904.3
Q_R, W	500.0
Q_e, W	419.7
Q_f, W	297.7
P_c, W	106.3
$\eta_{emitter}$, %	84.0
η_{filter}, %	70.9
η_{cell}, %	35.7
η_{RTPV}, %	21.3

The emitter maintained an average surface temperature of 904.3℃, with a spatial temperature distribution depicted in Fig. 6. Fig. 6c quantifies the thermal gradient profile, revealing a maximum localized gradient of 0.45 ℃·mm^{-1}. The temperature distributions of the PV array under these emitter temperature conditions are shown in Fig. 7.

The PV cell arrays exhibited a temperature range of 19.0 to 26.8℃, with a maximum temperature differential of 7.8℃. The spatial thermal analysis revealed a peak temperature gradient of 5.16℃·mm^{-1}, while 99.9 % of the surface area of the arrays-maintained gradients less than 5℃·mm^{-1}. These results demonstrate a highly uniform temperature distribution across the PV modules in the proposed computational model, with no detectable hotspot phenomena.

As is evident from Equations (7)-(12), temperature variations or inconsistencies in PV cell arrays altered their bandgap characteristics, inducing corresponding variations in key parameters such as the saturation current, (V_{oc}), and (J_{sc}), thereby affecting cell performance. Under idealized operating conditions with a uniform temperature distribution at an ambient level (10 °C), the PV cell arrays achieved a theoretical output power of 112.7 W (red curve in Fig. 8). However, under actual operating conditions with non-uniform temperature profiles (Fig. 7b), the total output power reduced to 106.3 W, incurring a 6.4 W loss (5.7 % reduction).

This degradation arose due to two key factors: (1) elevated surface temperatures of the module area, and (2) localized thermal gradients (max ΔT = 7.8 °C) inducing a current–voltage mismatch. As illustrated in Fig. 8, temperature increases predominantly affected the V_{oc}, which declined linearly at a rate of −1.4 mV/℃, while J_{sc} remained stable (±0.3 %). The resultant power loss followed a temperature coefficient of −0.34 %/°C, quantitatively linking thermal heterogeneity to system efficiency limitations.

4.2. Long-term performance evolution of the RTPV system

Fig. 9 shows the changes in the RTPV system and its components induced by the thermal power decay due to radioisotope source decay over a 50-year period. During the 50-year operational period, the RTPV system exhibited progressive thermal degradation. The emitter surface temperature decreased from 904.3 to 850.3 ℃, while the fuel pellet and cladding temperatures declined by 149.2 °C (from 1345.9 to 1196.7 ℃) and 181.2 ℃ (from 1258.6 to 1077.4 ℃), respectively.

Fig. 10 shows the efficiency changes, and the efficiency degradation included reductions of 15.2 % in emitter efficiency (from 83.97 to 68.73 %), 1.2 % in filter efficiency η_{filter} (from 70.91 to 69.68 %), and 4.4 % in system-level efficiency (from 21.27 to 16.89 %), with an average annual degradation rate of 0.22 %. With the attenuation of the radioisotope heat source, the temperature of the fuel pellet decreased annually, resulting in a decrease in the temperature of the emitter, and the radiant heat flux radiating outward at the emitter is reduced. Therefore, the emitter efficiency decreased significantly over time, while the temperature change of the emitter did not obviously change its spectral pattern, and the filter efficiency (η_{filter}) did not change significantly owing to the temperature of the emitter.

The electrical output power degradation profile and reliability assessment of the system are illustrated in Fig. 11. Accounting for the degradation of both the PV module and heat source, the power output decreased to 50 % of the initial value after 20 years, with PV reliability concurrently declining to 0.48. No significant reliability degradation was observed during the first 15 years; however, an abrupt decline

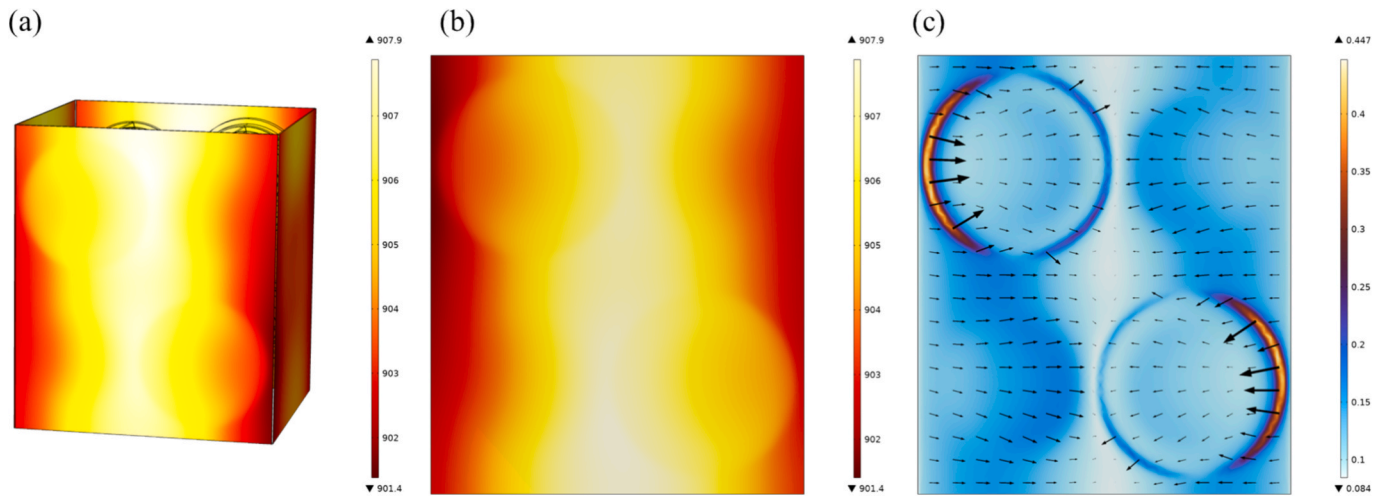

Fig. 6. (a) Temperature distribution of emitters, (b) temperature distribution of a single emitter, (c) thermal gradient corresponding to the configuration in (b).

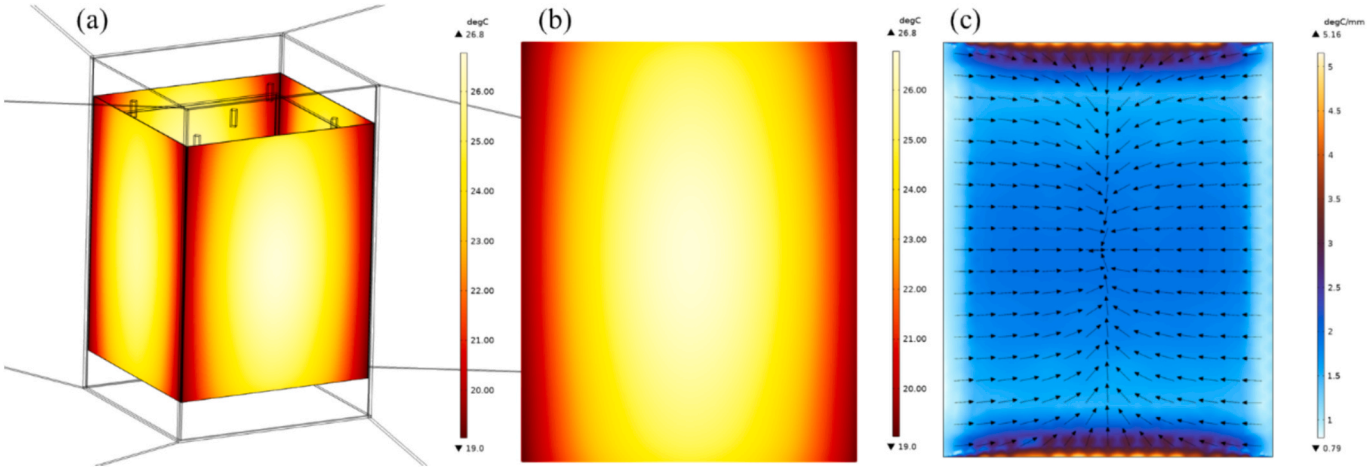

Fig. 7. (a) Temperature distribution of PV cell arrays, (b) temperature distribution of a single PV cell array, (c) thermal gradient corresponding to the configuration in (b).

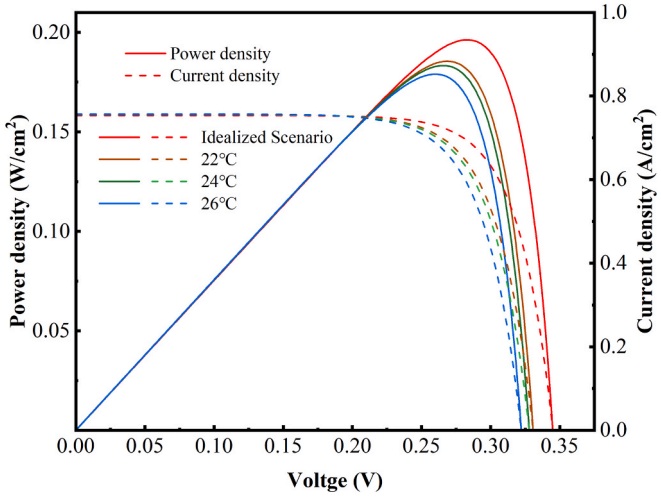

Fig. 8. Performance of the RTPV system.

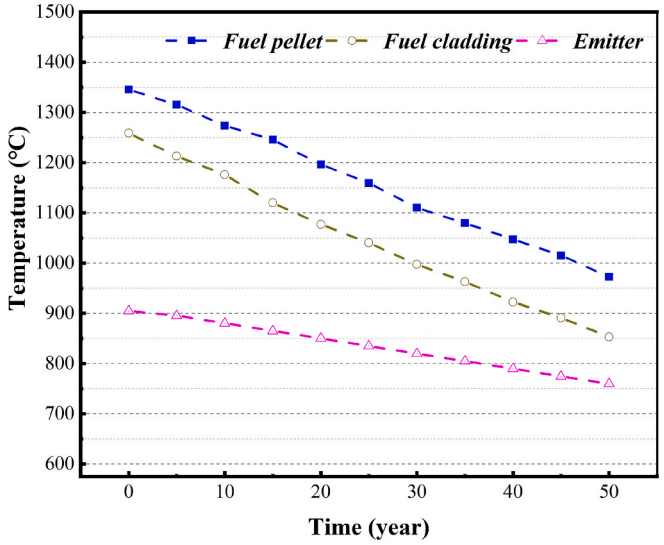

Fig. 9. Changes in system parameters over a 50-year period: average temperature of the fuel pellet, fuel cladding, and emitter.

commenced at year 16, culminating in complete failure (reliability = 0) by year 30. Despite a residual power output of ~ 37 W, the system was irreversibly compromised and unable to sustain power delivery to

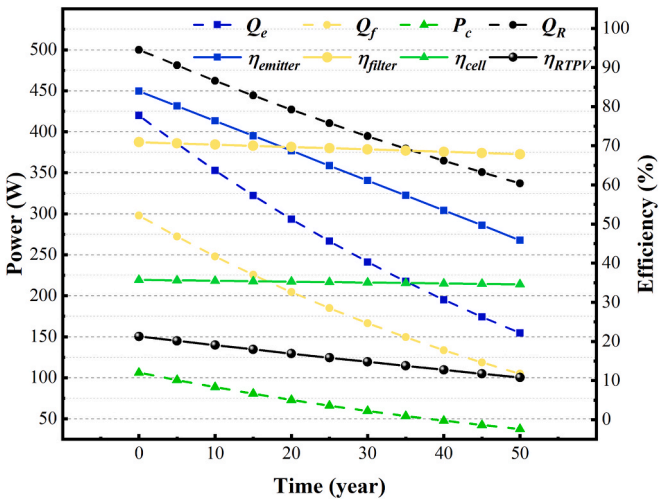

Fig. 10. Changes in system parameters over a 50-year period: thermal power of the radioisotope (Q_R), radiative heat flux emitted by the emitter (Q_e), radiative heat flux through the filter (Q_f), electrical output power generated by the InGaAs cells (P_c), emitter efficiency ($\eta_{emitter}$), filter efficiency (η_{filter}), cell efficiency (η_{cell}), and system efficiency (η_{RTPV}).

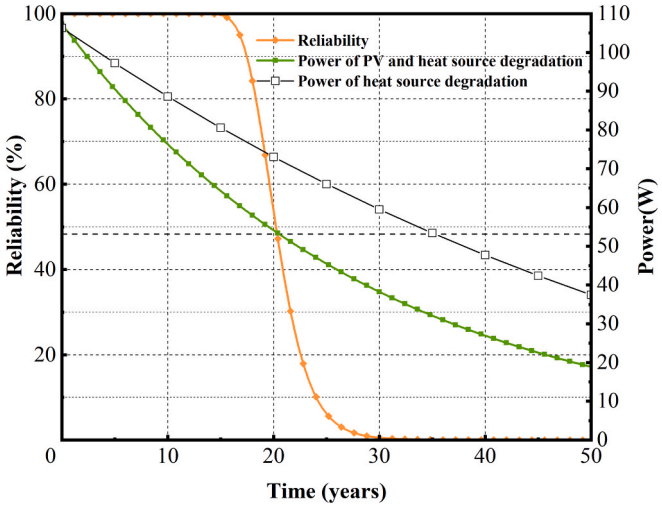

Fig. 11. Power degradation and reliability assessment of the model.

external devices. When explicitly incorporating PV aging effects, the theoretical power degradation accelerated: a 50 % reduction occurred within 20 years, culminating in complete system failure by year 30.

4.3. RTPV vs other RTG

Table 5 compares the performance metrics of different radioisotope power systems, including traditional RTGs (SNAP RTG, MHW RTG, GPHS RTG, MMRTG) and the RTPV system developed in this study. In terms of energy conversion efficiency, conventional RTGs show a relatively narrow range of 6.2–6.8 %, while the RTPV system achieves a remarkable 21.3 %, indicating much more efficient energy utilization. For initial output power, traditional RTGs have varied outputs (SNAP RTG: 2.7–63.5 W; MHW RTG: 158 W; GPHS RTG: 292 W; MMRTG: 123 W), and the RTPV system delivers 106.4 W. Regarding specific power, a key factor for space applications due to mass constraints, traditional RTGs range from 1.3-5.2 W/kg, whereas the RTPV system reaches 12.3 W/kg, showcasing significant mass – efficiency advantages. Overall, the RTPV system outperforms traditional RTGs in efficiency and specific power, presenting a promising option for space power supply despite its moderate initial output.

Table 5
Comparison of efficiency, power and specific power of different RTG, with RTPV [34].

Type	energy conversion efficiency (%)	Initial output power (W)	Specific Power (W/kg)
SNAP RTG	6.2 %-6.6 %	2.7–63.5	1.3–3.2
MHW RTG	6.6 %	158	4.2
GPHS RTG	6.8 %	292	5.2
MMRTG	6.3 %	123	2.8
This study	21.3 %	106.4	12.3

5. Conclusion

This study has presented a comprehensive design and analysis of a 500 W RTPV system based on dual GPHS modules, achieving breakthrough efficiency and longevity for deep-space power applications. The integrated COMSOL-MATLAB multi-physics model demonstrated exceptional predictive accuracy, with less than 1 % deviation in GPHS thermal simulations and a 0.1 % error in PV power calculations compared to experimental benchmarks. The system delivered an initial conversion efficiency of 21.3 %, driven by the optimized component efficiencies of 84.0 % for the emitter, 70.9 % for the spectral filter, and 35.7 % for the InGaAs PV arrays. Critical thermal management was achieved through controlled temperature gradients of 0.45 °C·mm^{-1} at the emitter surface (904.3 °C operational temperature) and less than 5 °C·mm^{-1} across 99.9 % of the PV array area (19.0–26.8 °C range), effectively eliminating hotspot risks while maintaining spectral matching stability. This thermal decline reduced the radiative flux (Q_e) by 51.3 % (419.7 → 204.3 W), accounting for 85.3 % of the total efficiency loss, while PV cell degradation contributed only 4.2 % due to the radiation-hardened InGaAs architecture. A novel hybrid degradation model, incorporating radioisotope decay kinetics and material aging mechanisms, predicted critical reliability thresholds of a 20-year power half-life (106.3 → 53.15 W) and complete functional failure at 30 years (R(t) = 0).

This work advances RTPV technology by demonstrating a 500 W system with 21.3 % initial efficiency and a multi-physics coupling framework for longevity assessment, critical for deep-space missions requiring decade-scale reliability. The hybrid degradation model, integrating radioisotope decay and material aging, provides a predictive tool for power decay (0.21 %/year) and operational thresholds (30-year failure). However, experimental validation under extreme thermal cycling and radiation environments remains outstanding. Additionally, the model assumes uniform material aging rates, potentially underestimating localized degradation in non-idealized space conditions. Future work should address scalability beyond 100-watt systems and incorporate irradiation-induced lattice defects to refine lifetime predictions for mission-critical deployments.

Declaration of competing interest

The authors declare that they have no known competing financial interests or personal relationships that could have appeared to influence the work reported in this paper.

Acknowledgements

This research was supported by the National Natural Science Foundation of China (Grant No. 12275132), and the prospective layout project of Nanjing University of Aeronautics and Astronautics (Grant No.

ILB240161A24).

Appendix A. Supplementary data

Supplementary data to this article can be found online at https://doi.org/10.1016/j.applthermaleng.2025.128087.

Data availability

Data will be made available on request.

References

[1] L. Xu, Y. Zou, Y. Jia, China's planning for deep space exploration and lunar exploration before 2030, Chin. J. Space Sci. 38 (2018) 591, https://doi.org/10.11728/cjss2018.05.591.

[2] W. Wu, W. Liu, D. Qiao, D. Jie, Investigation on the development of deep space exploration, Sci. China Technol. Sci. 55 (2012) 1086–1091, https://doi.org/10.1007/s11431-012-4759-z.

[3] E. Turan, S. Speretta, E. Gill, Autonomous navigation for deep space small satellites: scientific and technological advances, Acta Astronaut. 193 (2022) 56–74, https://doi.org/10.1016/j.actaastro.2021.12.030.

[4] M. Howell, V. Kodali, R. Segall, H. Aboudja, D. Berleant, Moore's law and space exploration: new insights and next steps, J. Arkansas Acad. Sci. 73 (2019), https://doi.org/10.54119/jaas.2019.7303.

[5] G. Stivers, Radioisotope thermoelectric space power supplies, IEEE Trans. Aerospace 2 (1964) 652–660, https://doi.org/10.1109/TA.1964.4319650.

[6] A. Barco, R.M. Ambrosi, H.R. Williams, K. Stephenson, Radioisotope power systems in space missions: overview of the safety aspects and recommendations for the European safety case, J. Space Saf. Eng. 7 (2020) 137–149, https://doi.org/10.1016/j.jsse.2020.03.001.

[7] X.-L. Shi, J. Zou, Z.-G. Chen, Advanced thermoelectric design: from materials and structures to devices, Chem. Rev. 120 (2020) 7399–7515, https://doi.org/10.1021/acs.chemrev.0c00026.

[8] J. He, T.M. Tritt, Advances in thermoelectric materials research: looking back and moving forward, Science 357 (2017) eaak9997, https://doi.org/10.1126/science.aak9997.

[9] J. Wei, L. Yang, Z. Ma, P. Song, M. Zhang, J. Ma, F. Yang, X. Wang, Review of current high-ZT thermoelectric materials, J. Mater. Sci. 55 (2020) 12642–12704, https://doi.org/10.1007/s10853-020-04949-0.

[10] Y. Liu, Y. Zhang, Q. Xiang, F. Hao, Q. An, H. Chen, Comprehensive modeling and parametric analysis of multi-mission radioisotope thermoelectric generator, Appl. Therm. Eng. 219 (2023) 119447, https://doi.org/10.1016/j.applthermaleng.2022.119447.

[11] X. Wang, R. Liang, P. Fisher, W. Chan, J. Xu, Critical design features of thermal-based radioisotope generators: a review of the power solution for polar regions and space, Renew. Sustain. Energy Rev. 119 (2020) 109572, https://doi.org/10.1016/j.rser.2019.109572.

[12] A. Datas, A. Martí, Thermophotovoltaic energy in space applications: review and future potential, Sol. Energy Mater. Sol. Cells 161 (2017) 285–296, https://doi.org/10.1016/j.solmat.2016.12.007.

[13] S.J. Cheon, S.G. Hong, Y.S. Nam, J.H. Lee, A radiation analysis of 500W RTPV system having cylindrical sources, in: EPJ Web of Conferences, Vol. 153, EDP Sciences, 2017, p. 04003, https://doi.org/10.1051/epjconf/201715304003.

[14] D.T. Cotfas, P.A. Cotfas, O.M. Machidon, Study of temperature coefficients for parameters of photovoltaic cells, Int. J. Photoenergy 2018 (2018) 5945602, https://doi.org/10.1155/2018/5945602.

[15] C. Sun, Y. Zou, C. Qin, B. Zhang, X. Wu, Temperature effect of photovoltaic cells: a review, Adv. Compos. Hybrid Mater. 5 (2022) 2675–2699, https://doi.org/10.1007/s42114-022-00533-z.

[16] R.C. O'Brien, R.M. Ambrosi, N.P. Bannister, S.D. Howe, H.V. Atkinson, Safe radioisotope thermoelectric generators and heat sources for space applications, J. Nucl. Mater. 377 (2008) 506–521, https://doi.org/10.1016/j.jnucmat.2008.04.009.

[17] Z. Wang, D. Kortge, Z. He, J. Song, J. Zhu, C. Lee, H. Wang, P. Bermel, Selective emitter materials and designs for high-temperature thermophotovoltaic applications, Sol. Energy Mater. Sol. Cells 238 (2022) 111554, https://doi.org/10.1016/j.solmat.2021.111554.

[18] U. Ortabasi, B. Bovard, Rugate technology for thermophotovoltaic (TPV) applications: a new approach to near perfect filter performance, in: AIP Conference Proceedings, Vol. 653, No. 1, American Institute of Physics, 2003, pp. 249–258, https://doi.org/10.1063/1.1539381.

[19] W.E. Horne, M.D. Morgan, V.S. Sundaram, IR filters for TPV converter modules, in: AIP conference proceedings, Vol. 361, No. 1, American Institute of Physics, 1996, pp. 993–1002, https://doi.org/10.1063/1.50002.

[20] S. Cao, Q. Cai, Y. Zhang, Q. Zhang, Q. Ye, W. Deng, X. Wu, Evaluation of spectral regulation by selective emitter and filter under both ideal and actual conditions for solar thermophotovoltaic systems, Renew. Energy 217 (2023) 119244, https://doi.org/10.1016/j.renene.2023.119244.

[21] E.S. Clarke, J. Giglio, K.J. Wahlquist, C.E. Dees, K.M. Geddes, J.C. Birch, S.E. Davis, B.M. Horkley, H.L. Usher, L.T. Rich, Multi-mission thermoelectric generator assembly testing and launch operations for mars 2020, in: Report Number: INL/CON-21-61664-Rev000, Research Org.: Idaho National Laboratory (INL), Idaho Falls, ID (United States), 26AD. https://www.osti.gov/biblio/1845446.

[22] W. Pardue, Heat source component development program. Quarterly report, October–December 1976, Battelle Columbus Labs., OH (United States), 1977. https://doi.org/10.2172/7119637.

[23] D.J. Senor, J.K. Thomas, K.L. Peddicord, Thermophysical property correlations for the niobium-1% zirconium alloy, J. Nucl. Mater. 173 (1990) 261–273, https://doi.org/10.1016/0022-3115(90)90394-3.

[24] D.R. Pantano, D.H. Hill, Thermal analysis of Step 2 GPHS for next generation radioisotope power source missions, in: AIP Conference Proceedings, Vol. 746, No. 1, American Institute of Physics, 2005, pp. 827–834, https://doi.org/10.1063/1.1867204.

[25] C.T. Or, E.A. Skrabek, Steady-state temperature predictions for general purpose heat source in vacuum, in: AIP Conference Proceedings, Vol. 420, No. 1, American Institute of Physics, 1998, pp. 1257–1262, https://doi.org/10.1063/1.54745.

[26] J.-Q. Li, X.-L. Xia, C. Sun, X. Chen, Q.-Y. Wang, Simultaneous measurement of normal spectral emissivity and temperature of materials with low thermal conductivity, Exp. Therm Fluid Sci. 148 (2023) 110966, https://doi.org/10.1016/j.expthermflusci.2023.110966.

[27] Q. Zhou, P. Wang, K. Wu, J. Cao, H. Zhang, Y. Zhang, B. Niu, D. Long, Performance of high-temperature lightweight multilayer insulations, Appl. Therm. Eng. 211 (2022) 118436, https://doi.org/10.1016/j.applthermaleng.2022.118436.

[28] H. Yu, M. Li, Y. Deng, S. Fu, J. Guo, H. Zhao, J. Zhang, S. Dang, P. Zhang, J. Zhou, D. Liu, D. Wang, C. Zhang, M. Hao, X. Xu, Chemically bonded multi-nanolayer inorganic aerogel with a record-low thermal conductivity in a vacuum, Natl. Sci. Rev. 10 (2023) nwad129, https://doi.org/10.1093/nsr/nwad129.

[29] T. Cai, Z. Xu, Y. Yi, C. Wang, B. Zhou, C. Chen, Y. Liu, Y. Wang, H. Lu, X. Tang, Advancing thermal radiation efficiency with hybrid-patterned metasurface emitters in thermophotovoltaic systems, Int. J. Therm. Sci. 213 (2025) 109790, https://doi.org/10.1016/j.ijthermalsci.2025.109790.

[30] J. Ajayan, D. Nirmal, A review of InP/InAlAs/InGaAs based transistors for high frequency applications, Superlattice. Microst. 86 (2015) 1–19, https://doi.org/10.1016/j.spmi.2015.06.048.

[31] A. Schock, M. Mukunda, T. Or, V. Kumar, G. Summers, Radioisotope thermophotovoltaic (RTPV) generator and its applicability to an illustrative space mission, Fairchild Space and Defense Corporation, 1994. https://doi.org/10.2172/1053502.

[32] M. Vázquez, I. Rey-Stolle, Photovoltaic module reliability model based on field degradation studies, Prog. Photovolt. 16 (2008) 419–433, https://doi.org/10.1002/pip.825.

[33] S. Shiri, A robust optimization approach for design of a General Purpose Heat Source, J. Space Saf. Eng. 8 (2021) 211–216, https://doi.org/10.1016/j.jsse.2021.07.006.

[34] G.R. Schmidt, T.J. Sutliff, L.A. Dudzinksi, Radioisotope power: a key technology for deep space exploration, Radioisotopes-Appl. Phys. Sci. (2011) 419–456, https://doi.org/10.2514/6.2008-5640.